V–O–C Bonding of Heterointerface Boosting Kinetics of Free-Standing Na$_5$V$_{12}$O$_{32}$ Cathode for Ultralong Lifespan Sodium-Ion Batteries

Xuexia Song, Xifei Li,* Hui Shan, Jingjing Wang, Wenbin Li, Kaihua Xu, Kun Zhang, Hirbod Maleki Kheimeh Sari, Li Lei, Wei Xiao, Jian Qin, Chong Xie, and Xueliang Sun*

The flexible free-standing cathodes with high energy density have been challenging toward wearable sodium-ion batteries (SIBs). Herein, Na$_5$V$_{12}$O$_{32}$ nanobelts (NVO-NBs)-based heterostructure is fabricated with boosting the sodium-ion kinetic characteristics to address the challenges. In the heterostructure, the controllable V–O–C bonds are generated at the interface originating from the chemical conversion of functional groups of the reduced graphene oxides (rGOs) with V–O bonding of NVO through interfacial electronic interactions. The interfacial synergistic between the brilliant bonding properties and the inherent formation of a stress field at the heterointerface motivated by work function difference can reduce the Na$^+$ diffusion barrier, facilitate charge transfer, hence accelerates reaction kinetics and electron/ion transport, as well as modifying the electronic structure to realize a cherished adsorption energy of Na$^+$. Therefore, the optimized NVO-NBs-based heterostructure exhibits exceptional rate capability (213 mAh g^{-1} at 0.2 C with 100 mAh g^{-1} at 10 C) and ultralong cycling stability (95.4%, 3000 cycles at 5 C). This work demonstrates that the controllable heterostructure interface with abundant chemical bonds is an effective approach to exploit potential cathodes for rechargeable batteries.

1. Introduction

Vanadium-based compounds possess multivalent states of vanadium (from V^{2+} to V^{5+}) and a wide interplanar spacing, which provides more possibilities to further extend their specific capacities by enabling the reversible Na$^+$ intercalation/deintercalation.[1–8] Among them, in numerous reports, sodium vanadium oxides have displayed satisfying capacities acting as cathode of SIBs when operated in a wider voltage window (1.5–4.0 V).[9–16] In our previous work, the sodium vanadium bronze (NaV$_6$O$_{15}$) nanotubes of clew-like carbon-coated were designed, which could supply an exceptional capacity of 209 mAh g^{-1} at 25 mA g^{-1}.[7] Furthermore, a K$^+$-doped sodium vanadate (Na$_{5-x}$K$_x$V$_{12}$O$_{32}$) cathode was synthesized with a reversible capacity of 169 mAh g^{-1} at 26 mA g^{-1}.[8] Dong et al. also synthesized hierarchical

X. Song, X. Li, H. Shan, J. Wang, W. Li, H. M. K. Sari, L. Lei, W. Xiao, J. Qin, C. Xie, X. Sun
Shaanxi International Joint Research Center of Surface Technology for Energy Storage Materials
Institute of Advanced Electrochemical Energy & School of Materials Science and Engineering
Xi'an University of Technology
Xi'an, Shaanxi 710048, P. R. China
E-mail: xfli@xaut.edu.cn; xsun9@uwo.ca

K. Xu, K. Zhang
GEM Co., Ltd.
Shenzhen 518101, P. R. China
X. Sun
Department of Mechanical and Materials Engineering
University of Western Ontario
London, Ontario N6A 5B8, Canada

**ADVANCED
SCIENCE NEWS**

www.advancedsciencenews.com

**ADVANCED
FUNCTIONAL
MATERIALS**

www.afm-journal.de

zigzag $Na_{1.25}V_3O_8$ nanowires that showed the capacity of 172.5 mA h g^{-1} at 100 mA g^{-1}.[9] Indeed, the $Na_{1.1}V_3O_{7.9}$ nanobelts assembled by Yuan et al. showed the capacity of 173 mA h g^{-1} at 25 mA g^{-1}.[11]

These abovementioned vanadium-based materials still endure inferior electrical conductivity, resulting in limited cycling stability as well as inferior rate ability due to the structural collapse and capacity fading.[11–16] To tackle these concerns, some approaches have been adopted, such as constructing hierarchical structures to boost Na-ion diffusion kinetics,[9–15] recombining with carbon materials (e.g graphene, carbon nanotube) in order to enhance the electrical conductivity,[15–17] and designing unique heterostructures to alleviate interfacial strain and enhance reaction kinetics.[18] Heterostructures are a valuable approach to intensify the ion storage, which is extensively applied in various energy storage devices.[19–24] The fabrication of heterostructures relating to interface modification strategies presents feasible avenues for electronic/ionic delivery, maintaining structural stability as well as stimulating more storage sites. The researchers have probed chemical bonding at the hetero-interface among transition metal oxides.[25–26] The $La_{0.8}Sr_{0.2}MnO_{3-y}$ (LSM)-coated $Li_{1.2}Ni_{0.13}Co_{0.13}Mn_{0.54}O_2$ (LM) displays an improved capacity of 202 mAh g^{-1} at 1 C with remarkable electrochemical performance.[25] The Mn–O–M bonded at the LSM/LM interface can reduce the dissolution of Mn, which avoids the layered-spinel evolution. Na-ion half-cells using MoO_2/N-doped carbon (MoO_2/N-C) with a Mo–N–C chemical bond display superior cyclability over 5000 cycles at 5 A g^{-1} and excellent rate capability.[26] It can be concluded that the establishment of interfacial chemical bonding is essential to advance charge aggregations at the interface. Therefore, it is enormously expected to investigate the interfacial chemical bonding to simultaneously boost the interfacial and surface reaction kinetics.

Herein, a free-standing $Na_5V_{12}O_{32}$-rGO heterostructure with a controllable V–O–C bond was elegantly arranged to act as the cathode with a highly efficient sodium-ion storage and ultralong cycling stability. The generated V–O–C bond could reinforce the structural stability, strengthen the interfacial ion transport and even boost conductivity. Further accelerate reaction kinetics. Meanwhile, the bonds could efficiently modify the electronic structure to realize cherished adsorption energy of Na$^+$. The electrochemical mechanism is uncovered based on surface-dominated charge storage at the interface, leading to a unique interfacial pseudo-capacitance,[27–28] which is different from the "job-sharing" mechanism on the basis of the capability of thermodynamics.[29–31]

2. Results and Discussion

The crystal structure of the as-prepared material was investigated via the X-ray diffraction (XRD) patterns together with the Rietveld refinement, as shown in **Figure 1**a–c. Figure 1a displays XRD patterns of the NVO, NVO/rGO, and NVO-rGO membranes. It can be observed that the composition of materials is determined as the mixture of $Na_5V_{12}O_{32}$ and NaV_3O_8 phase, among which, most of them could be well catalogued to the monoclinic structure of $Na_5V_{12}O_{32}$ (JCPDS no. 24–1156). A few additional weak diffraction peaks can be observed, which can be corresponded to the NaV_3O_8 (JCPDS no. 12–0676, marked with an asterisk). It suggests that a little NaV_3O_8 impurities are generated. The

main diffraction peaks of the three samples are situated at 7.6°, 12.6°, and 27.6°, corresponding to the reflections of (100), (001), and (011) of $Na_5V_{12}O_{32}$. The Figure 1b shows an enlargement within the 2θ range of 20–35°. The enlarge XRD patterns show that the diffraction peak located at 28.6° and 29.6° can match well with $Na_5V_{12}O_{32}$ phase, which correspond to (102) and (−401) lattice planes. Besides, the diffraction peaks locating at 13.3°, 34.4°, and 41.5° corresponding to NaV_3O_8 phase, the sample has lower peak apex, which indicates that the NaV_3O_8 phase has low crystallinity. Therefore, all representative diffraction peaks of the three materials can be catalogued to the major monoclinic phases of sodium vanadate (i.e., $Na_5V_{12}O_{32}$ and $Na_{1.25}V_3O_8$). The NVO/rGO and NVO-rGO electrodes present a similar diffraction tendency to those of the pure NVO sample, implying that NVO maintain its structure well during combining with rGO. An additional small and broad diffraction peak appears at 26.5° in the composite materials, which can be indexed to the peak of $Na_5V_{12}O_{32}$ coinciding with the peak of graphene sheet.[9]

Retrieved refinement was performed utilizing the GSAS II program, the obtained fitted XRD diagram accords well with the standard card (JCPDS no. 24–1156) (Figure 1c) because the calculated pattern (red line) is very analogous to the experimental result (black circles) ($R_p = 10.2\%$, $\chi^2 = 1.518$). The corresponding lattice parameters of $Na_5V_{12}O_{32}$($Na_{1.25}V_3O_8$) after refinement are $a = 12.14$ Å, $b = 3.61$ Å, $c = 7.32$ Å, and $\beta = 106.73°$. It indicates that the achieved materials possess a fairly pure phase with a space group: $P21/m$. About five percent of impurity phases (NaV_3O_8) was detected in the sample, matching the fitted XRD pattern (Figure 1c). Although some peaks are close, it is noted that $Na_5V_{12}O_{32}$ (JCPDS No. 24–1156) belongs to the major phase, NaV_3O_8 phase is ignored in the following discussions due to their relatively dominant content, because the undesirable impurities not affect battery performance to some extent, as we expected in the following discussion. As depicted in the crystal structure model shown in Figure 1c inset. It demonstrates that $Na_5V_{12}O_{32}$($Na_{1.25}V_3O_8$) is predominantly composed of the layers of V_3O_8 polyhedra, in which the chains of VO_5 pyramids and VO_6 octahedra extend across the axis through corner-yield oxygen atoms. In addition, the Na$^+$ ions principally occupy entire octahedral positions and the extra Na$^+$ ions are arrayed at tetrahedral positions with a certain possibility. Na$^+$ ions could be arranged at the active sites between interlayers during discharge, affording a satisfactory specific capacity.[16]

To demonstrate the vibration mode of V–O–C bond, FTIR spectra of as-prepared NVO-rGO, NVO/rGO, and pure NVO samples are shown in Figure 1d. Apparently, the absorption bands for all samples have a similar vibration mode. The peak positioned at 992 cm^{-1} is assigned to asymmetric stretching vibrations of V = O bond, and the peaks at 554 and 759 cm^{-1} are assigned to symmetric stretching vibrations of V–O–V, respectively.[15,16,32] Compared with the NVO/rGO and NVO samples, slight blue shift of V = O stretching bond in NVO-rGO could be attributed to the connections between NVO (positive V) and rGO (negative O). However, the pronounced red movement for the V–O–V suggests that carbon atom of rGO might firmly bind with the oxygen atom on the NVO NBs surface to form a V–O–C atom-scale interface.

Raman spectra of NVO-rGO, NVO/rGO, and NVO samples are displayed in Figure 1e,f. Both composite samples exhibit typical peaks of rGO (the peak of D-band and G-band at about
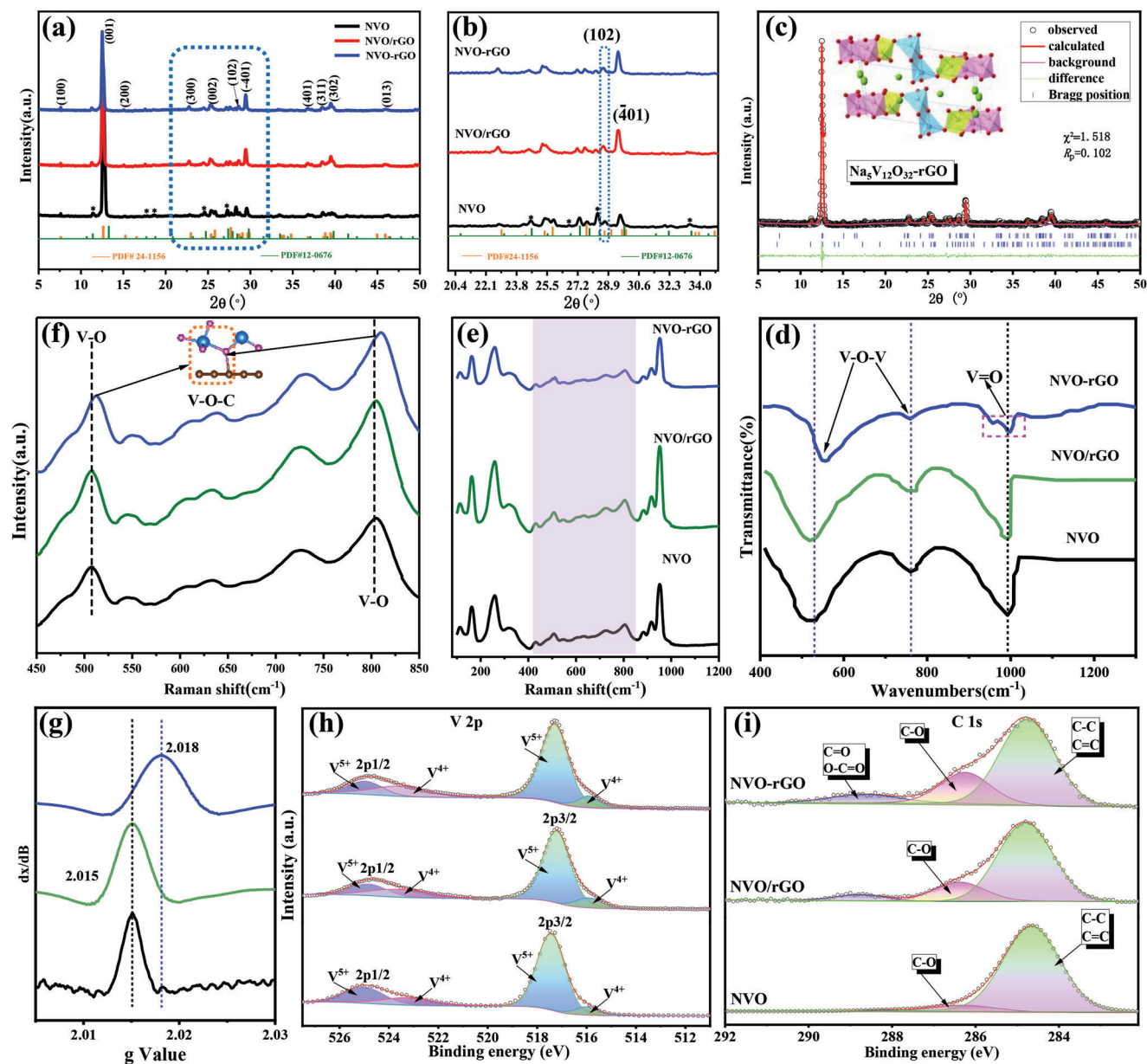
Figure 1. a,b) XRD patterns of NVO, NVO/rGO and NVO-rGO samples; c) Retrieved refinement of NVO-rGO sample; d) FTIR spectra, e,f) Raman spectra; g) EPR spectra; h,i) The High-resolution XPS spectra of V 2p and C1s for the NVO-rGO, NVO/rGO and NVO.

$1350 \, cm^{-1}$ and $1580 \, cm^{-1}$) (Figure S3a, Supporting Information), and the values of I_D/I_G of rGO, NVO/rGO, and NVO-rGO are ≈1.01, 1.04, and 1.12, respectively. The high value of I_D/I_G illustrate that the NVO-rGO composites show a more disordered structure than NVO/rGO and rGO, which is beneficial for enhancing the electrical conductivity of the NVO-rGO, and it could manifest the generation of V−O−C bonds. Notably, G-band positions in NVO-rGO vary from those in NVO/rGO, demonstrating that the electron-phonon connection of graphene is improved in NVO-rGO sample.[33] This was confirmed by the difference between g-values of NVO-rGO sample with those of the NVO/rGO and NVO samples according to the EPR spectra (Figure 1g).The V−O−C bonding of NVO-rGO heterostructure was further veri-

fied when it revealed different g-value from NVO/rGO and NVO in the electron paramagnetic resonance(EPR) image, implying that V-O-C heterogeneous bonds lead to a change in the spin state of the lone electron of vanadium. The position at $806 \, cm^{-1}$ is ascribed to atomic movement of the corner-sharing oxygen between Na+ ions and the VO_6, VO_5 polyhedra, which matches the previous reports.[26,34–35] Indeed, the peaks at 731 and $955 \, cm^{-1}$ are ascribed to the $V = O$ and V−O−V vibrations while the peak at $262 \, cm^{-1}$ arises from the interaction of sodium and oxygen. From the enlarged view (Figure 1f), the peaks related to V−O stretching vibrations move to higher wave-numbers for NVO-rGO compared to those for the NVO/rGO and NVO.[36,37] The conclusions imply that there are additionally fabricated C−O bonds in
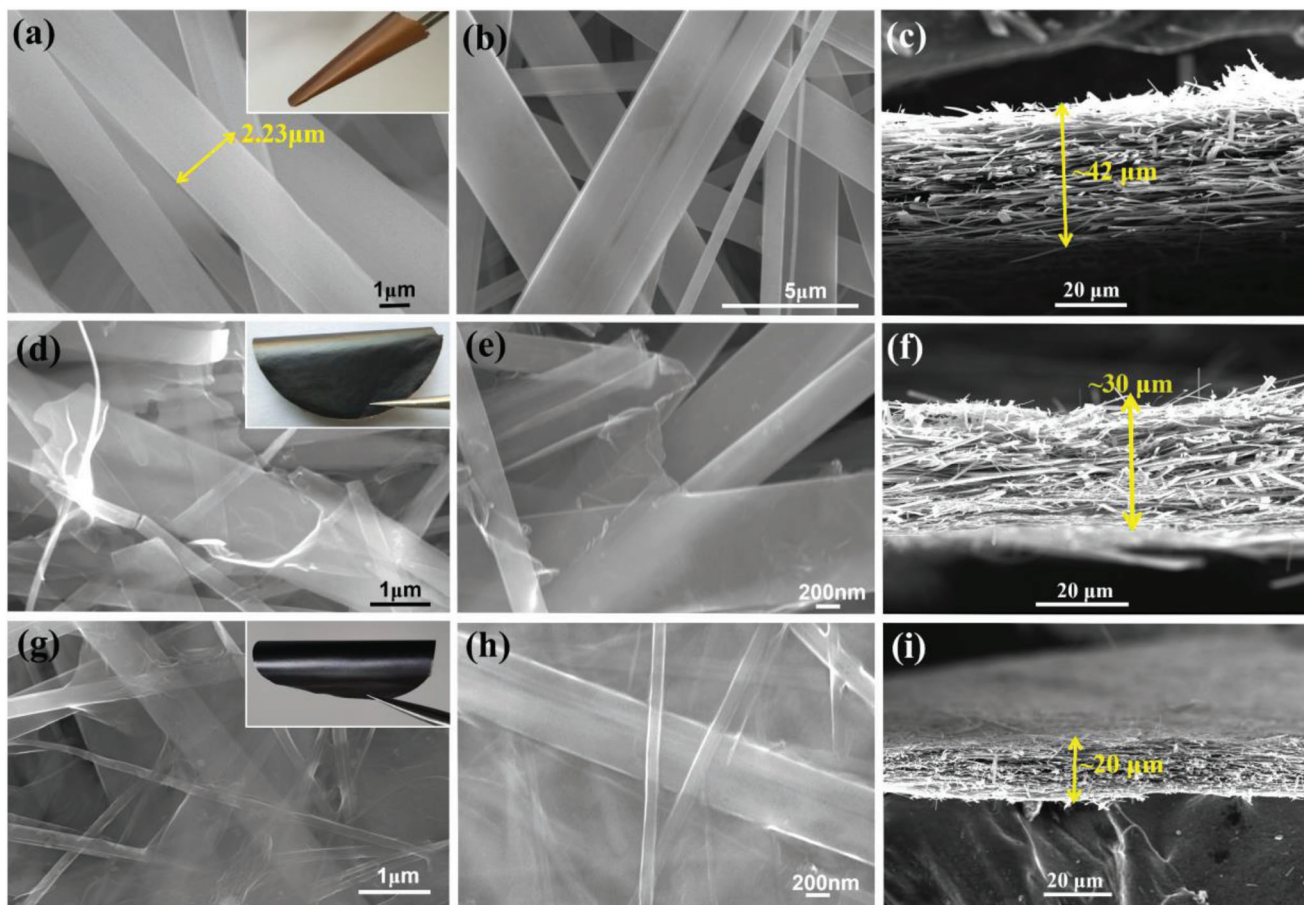
ADVANCED
SCIENCE NEWS

www.advancedsciencenews.com

ADVANCED
FUNCTIONAL
MATERIALS

www.afm-journal.de

Figure 2. The top-view and cross-sectional SEM images of the free-standing flexible film electrode at different magnifications (under the same quality): a–c) NVO. d–f) NVO/rGO. g–i) NVO-rGO. Insets show the flexible bent membrane electrodes (brown: NVO, black: NVO/rGO and NVO-rGO).

NVO-rGO sample, further demonstrating the generation of the V−O−C at the interface.

A measurement of X-ray photoelectron spectroscopy (XPS) was executed to explore the chemical valence of the elements (Figure S3b, Supporting Information). High-resolution XPS spectra of V2p signal of the materials are displayed in Figure 1h. As illustrated, peaks that are situated in 517.4 and 524.8 eV matching with the binding energies of $V2p_{3/2}$ and $V2p_{1/2}$, individually. After fitting the XPS via the XPS peak 4.1, the results are shown in Figure 1h, it can be clearly seen that the fitted peaks are divided into two sets of peaks belonging to V^{5+} and V^{4+}. Evidently, the positions at 517.4 eV and 524.8 eV correspond to $V^{5+}2p_{3/2}$ and $V^{5+}2p_{1/2}$, while the positions at 515.8 eV and 523.4 eV with lower intensity correspond to the $V^{4+}2p_{3/2}$ and $V^{4+}2p_{1/2}$.[38] The finally fitted areas of the V^{5+} and V^{4+} components can be used to detect the proportion of V^{4+} in the samples. The area proportion of V^{4+}/V^{5+} is estimated to be 1/11, which matches the proportion (0.909) in the shown chemical formula, i.e., $Na_5V^{4+}V^{5+}_{11}O_{32}$. High-resolution C1s spectrum (Figure 1i) could be resolved into three components: the primary position centered at 284.6 eV corresponds to C−C and C = C, whereas the peaks at 286.3 and 288.7 eV can be ascribed to C = O, C−O, and O−C = O, respectively.[39–40] It is evident that the C-O content in the NVO-rGO is clearly higher than that in NVO/rGO

and NVO, which is consistent with the Raman and FTIR spectra (Figure 1d–f). These results reveal that some C−O bonds are generated in the NVO-rGO heterostructure. The binding energy of V and O as detected by the XPS spectra implies the generation of V−O−C bonding in the NVO-rGO composites.[22–24,37] These results indicate that NVO NBs are chemically bonded with the rGO rather than simply physical intercontact.

Figure 2 exhibits the Scanning Electron Microscope (SEM) images of the free-standing membranes. After the filtration, the NVO, NVO/rGO, and NVO-rGO composites have turned to free-standing membranes without applying any binder (Figure S4, Supporting Information). Figure 2a,b reveal the top-view SEM Figure of the NVO NBs electrode. It can be observed that the membrane consists of nanobelts with 100–565 nm in width, which are distributed randomly and interweaved with each other to construct a network texture. The cross-sectional SEM manifests that the membrane has a thickness of ≈42 μm (Figure 2c). Comparatively, in the NVO/rGO membrane, owing to rapidly filtrating the mixed NVO and rGO dispersion, the NVO nanobelts and rGO nanosheets (NSs) exhibit a weak intercommunication and accumulate separately(Figure 2d,e). As it appears, the composite membrane is inhomogeneous with a thickness of 30 μm (Figure 2f). Figure 2g,h show the surface morphology of the NVO-rGO membrane. It can be observed that thin rGO NSs have

2303211 (4 of 15)

**ADVANCED
SCIENCE NEWS**

www.advancedsciencenews.com

**ADVANCED
FUNCTIONAL
MATERIALS**

www.afm-journal.de

tightly wrapped the NVO NBs to establish a dense structure, demonstrating a favorable hierarchical configuration. Figure 2i reveals that the composite membrane is 20 μm in thickness, and the NVO NBs and rGO NSs interlace with each other to form a multilayered stacking structure, signifying the good interaction between them. The good integrity of the NVO NBs and rGO NSs in the NVO-rGO membrane is confirmed as no separated rGO NSs can be observed on the surface (Figure 2g). Nonetheless, some separated rGO NSs are presented in the NVO/rGO membrane (Figure 2d), which has a mass ratio of rGO similar to that of the NVO-rGO membrane (≈9%). A tight fitting between the NVO NBs and rGO NSs may be beneficial for the cycling performance.[40] All the composite membranes can bend and roll (Figure 2a,d, and g inset). The engineering tensile stress and strain curves are displayed in Figure S4g (Supporting Information). Notably, it achieves a significant improvement on tensile stress even in the presence of a small amount of rGO NSs. For the NVO-rGO membrane, all of these properties are higher than those of other membranes, including tensile strength and toughness. Additionally, it can recover to its initial state after following bending (bending angle is ≈360°) as well as compressive deformation, indicative of its excellent elasticity, illustrating that the composite membranes are mechanically robust (Figure S4g, Supporting Information). The robust and flexible texture allows the NVO-rGO membrane to readily roll up without any visible fracture (Figure S4, Supporting Information). Figure S5 (Supporting Information) displays the EDX mapping images of all membranes. The conclusions confirm that the Na, O, V, and C are well sprinkled in NVO-rGO membrane (Figure S5j–s, Supporting Information).

The detailed structure of the NVO-rGO membrane was analyzed utilizing transmission electron microscopy (TEM) and high-resolution TEM (HRTEM). It is observed that straight and uniform NVO NBs are 100–565 nm in width (**Figure 3**a). HRTEM images of the NVO-rGO (Figure 3b,c) reveal that the lattice spacing of NVO nanobelts(the white pane selected region) is 0.392, 0.368, and 0.313 nm (Figure 3c), corresponding to the (300), (−102), and (102) lattice planes, respectively (Figure 3b). The selected area electron diffraction (SAED) image shown in Figure 3b (inset) suggests that the NVO NBs are single crystallinity. As shown in the TEM image (Figure 3d) of the NVO-rGO membrane (the green pane selected region), it is obvious that rGO is uniformly coated onto NVO NBs. In the HRTEM image of the region indicated by the arrow (Figure 3e), the rGO nanosheet is observed to possess multiple layers with an interlayer distance of 0.362 nm. Additionally, Energy-dispersive X-ray spectroscopy (EDS) was executed to qualitatively analyze the distribution of elements in as-prepared sample. EDS spectrum of the rectangular region (Figure 3d inset) exhibits that Na, V, and O co-exist in the NVO-rGO membrane, while only a small amount of carbon is detected (Figure 3f). The definite molar proportion of Na/V in the NVO NBs was determined to be 0.426 from the ICP-AES analysis, close to that (0.417) in the chemical formula of $Na_5V_{12}O_{32}$.

The high angle annular dark-field scanning transmission electron microscopy (HAADF-STEM) and annular bright field scanning transmission electron microscopy (ABF-STEM) technique was used to comprehend the atom evolution of the V–O–C interface. Figure 3g–i shows a set of bright and dark spots that could be detected as well as their structural characteristics. The FFT

analysis of (Figure 3k) the selected rectangular region(Figure 3i) and corresponding intensity profile (Figure 3l) demonstrates the typical layer atomic configurations without distortion of the structure, which are highly consistent with the atomic models(Figure 3j). The measured adjacent layer spacing of 3.92 Å and 3.68 Å in ABF-STEM images (Figure 3h) matches well with the HR-TEM results. It indicates that the formation of V–O–C does not alter the atomic configurations, but only slightly increases in the layer spacing, thus approving improved interaction behavior between layers and greater stability of the crystal arrangement.

Figure 4a reveals the cyclic voltammogram (CV) profiles of the NVO, NVO/rGO, and NVO-rGO within 1.5–4.0 V (vs Na^+/Na) at 0.1 mV s^{-1}. Apparently, the NVO-rGO exhibits stronger redox peak currents and larger integral area than those of other two electrodes, demonstrating that the construction of the NVO-rGO heterostructures dramatically improves the specific capacity and redox reaction kinetics. As illustrated in the CV plot (Figure 4a), two pairs of well-defined sharp and symmetrical redox peaks (at 2.40/2.60 V and 3.36/3.42 for the NVO-rGO; 2.38/2.60 V and 3.33/3.43 for the NVO/rGO; 2.36/2.66 V and 3.34/3.46 V for the NVO) appear on three electrodes, which is generally attributed to the Na^+ ion extraction and insertion from the NVO lattice matrix. It can be more evidently noticed in dQ/dV curves (Figure S6a–c, Supporting Information), with a redox potential difference (ΔV) of ≈0.05 V and 0.03 V for the NVO-rGO in dQ/dV curves. Notably, the larger ΔV values are conducted as ≈0.1 V/0.07 V for the NVO/rGO and ≈0.14 V/0.11 V for the NVO, respectively. Compared to the NVO-rGO, the oxidation and reduction peaks of the NVO and NVO/rGO electrodes shift toward lower and higher potentials, respectively, while there are no apparent distinction in the consequent cycles. Notably, the asymmetric and reduced redox peaks depicted in the NVO's plot implies its sluggish kinetics. The CV curves and dQ/dV curves of the three electrodes (Figure S6a–c, Supporting Information) also indicate lower electrochemical polarization and higher reversibility of the NVO-rGO electrode. The result is further illustrated in the galvanostatic charge-discharge (GCD) measurement at 0.1 C (26 mA g^{-1}): the GCD curves of the three samples exhibit similar charge/discharge voltage plateaus (Figure 4b). All explored voltage platforms are well matched and the redox peaks in the CV profiles. Furthermore, NVO-rGO presents a higher specific capacity, considerably exceeding that of the other two samples. Indeed, the decreased polarization and advanced redox kinetics are striking for the NVO-rGO electrode, profiting from the synergistic collaboration from the introduction of rGO and formation of the V–O–C bonding.

The cycling performance of all samples at 3 C is shown in Figure 4c. It is found that the NVO-rGO retains 97.6% of the original capacity after 1000 cycles, which is grander than those of the NVO/rGO (75.2%) and NVO (65.2%). The rate performance of all samples is displayed in Figure 4d. When the current density grows from 0.2 C, 0.5 C, 1 C, 3 C, 5 C to 10 C (2600 mA g^{-1}), the NVO-rGO electrode release the specific capacities of 213, 207, 192, 168, 145, and 100 mAh g^{-1}, respectively; Additionally, the reversible capacity nearing the original value could be obtained while it comes back to 0.2 C. Even at 10 C, the NVO-rGO electrode preserves a specific capacity of 100 mAh g^{-1}, while those of the NVO/rGO and NVO electrodes slide down to 66.4 and 21 mAh g^{-1}, respectively. The outcomes illustrate that the
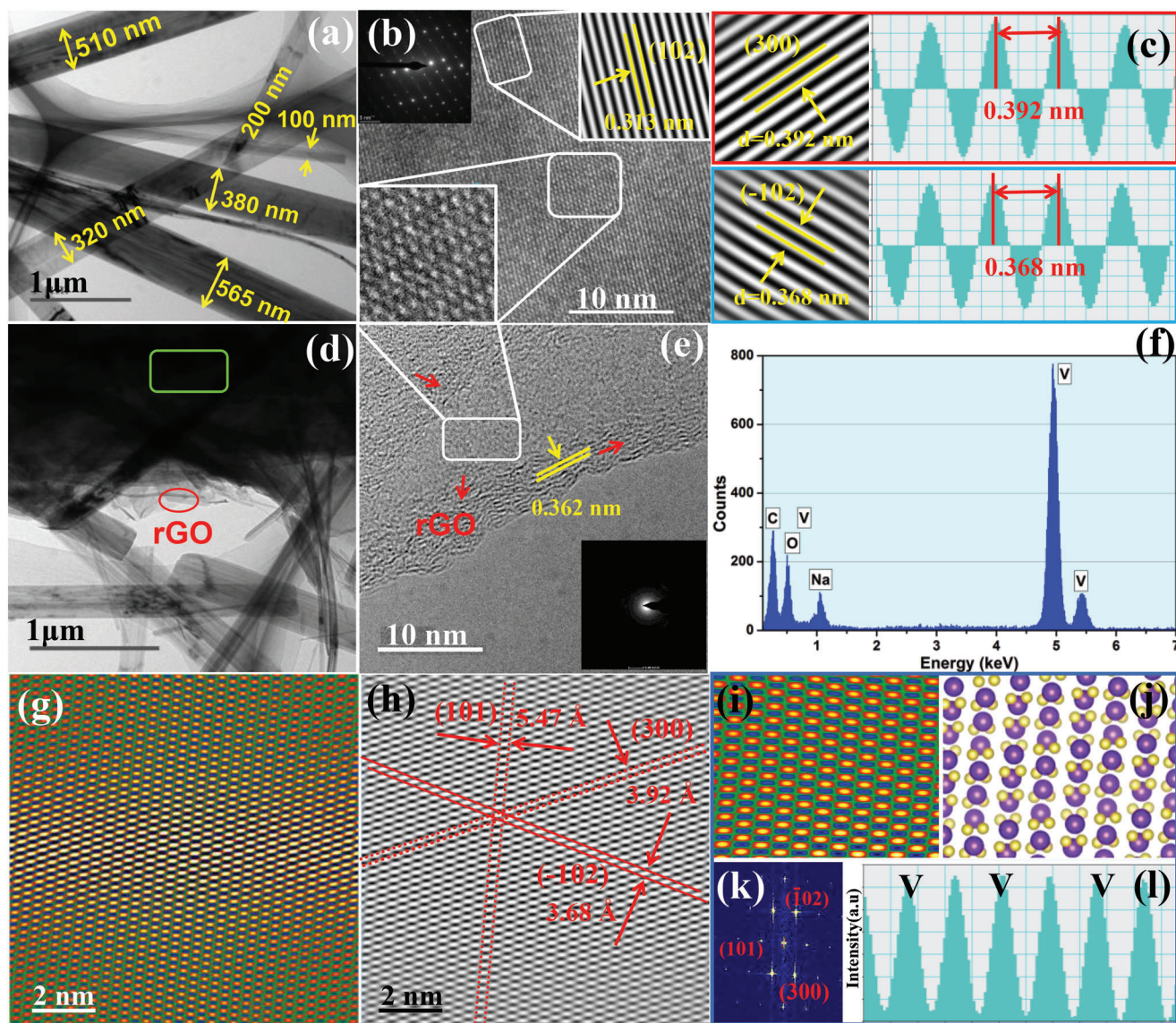
Figure 3. TEM images of the NVO-rGO composites: a,d) TEM images of NVO NBs and NVO-rGO composites; b,e) HRTEM image from the selected area as well as SAED (insets); c) IFFT image and the lattice spacing of NVO and NVO-rGO composites; f) EDS spectrum pattern of NVO-rGO composites. Atomic structure of the NVO-rGO composites: g,i) HAADF-STEM and enlarged pattern. h) ABF-STEM image and k) FFT patterns. j) The superimposed atomic array indicates the locations of each atom in NVO (Na [yellow], V [purple]). l) Line profile extracted across the interface with (i).

NVO-rGO is preferable in comparison to the NVO and NVO/rGO electrodes with regard to rate capability.

To modify the interfacial sodium-ion storage in the NVO-rGO heterostructures, three ratios of rGO were applied in the composite materials, and the resultant composites were electrochemically compared. As known to all, carbon ratio is an significant aspect influencing the electrochemical performance. The enhancement of rGO percentage can enhance the conductivity, but decrease the capacity of the cathode. Based on the TGA curves (Figure S2b, Supporting Information), the obtained three samples consisting of 4%, 9%, and 13% of rGO were labeled as the NVO-4% rGO, NVO-9% rGO, and NVO-13% rGO, respectively. As displayed in Figure S7 (Supporting Information), a large amount of NVO nanobelts interweave

and connect with rGO nanosheets to form a gathering structure (Figure 2). Uniform rGO nanosheets can be obviously noticed on the samples' surface, in which the rGO nanosheets are tightly anchored on the surface of NVO nanobelts, manufacturing an integrated network with the dominant content of NVO nanobelts. SEM images from the surface of NVO-9% rGO present a robust interconnected structure with a uniform distribution of rGO on the NVO network. However, when much more rGO nanosheets are introduced, a slight rGO aggregation can be discovered in the NVO-13% rGO (Figure S7d, Supporting Information).

To reflect the capacity contribution during the cycling of the NVO-rGO composite materials, the differential capacity curve method was prepared. Comparison between the differential
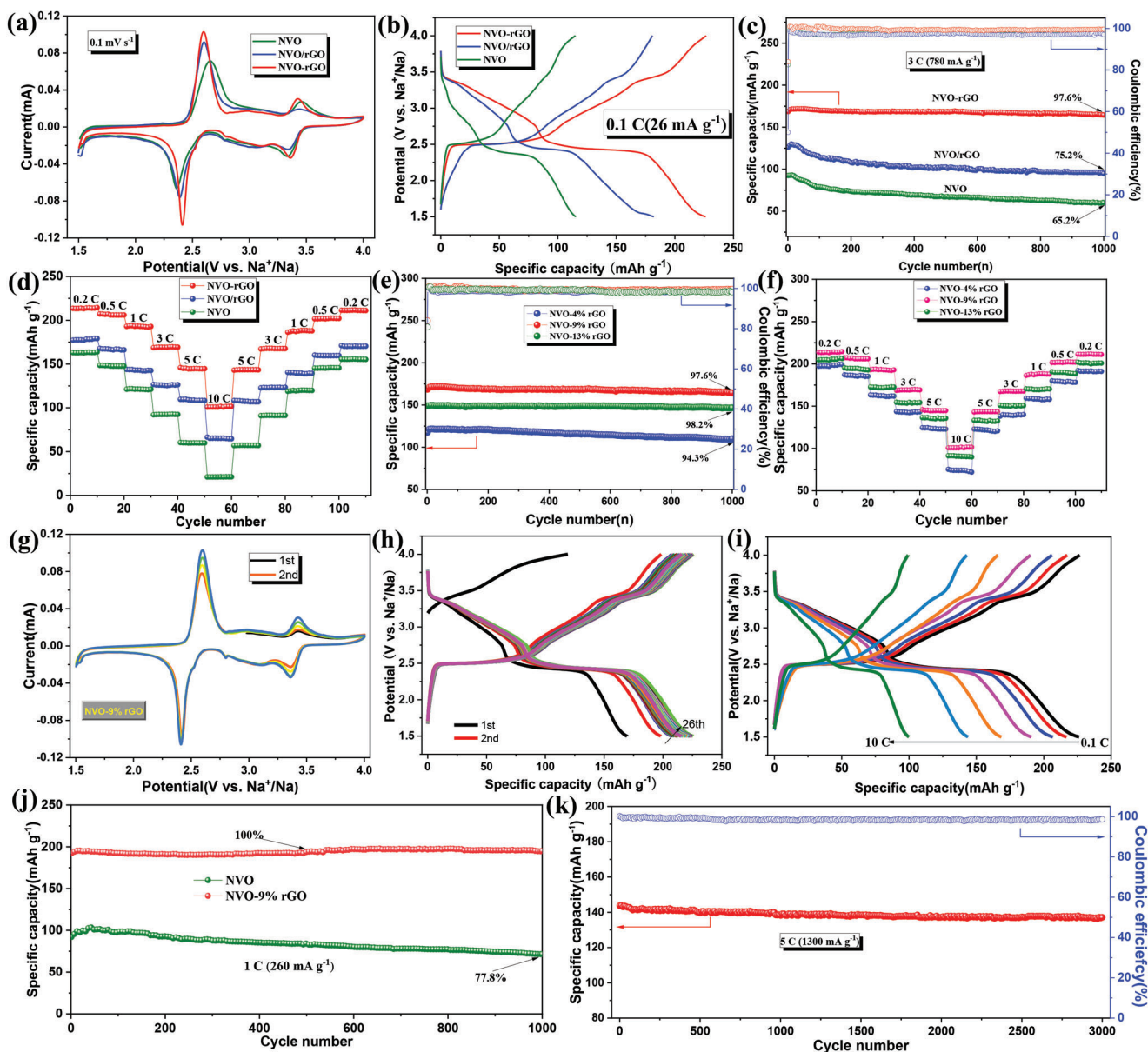
Figure 4. a–f) Electrochemical performance of the NVO, NVO/rGO, and NVO-rGO for SIBs: a) CV curves (0.1 mV s^{-1}) within 1.5–4.0 V (vs Na$^+$/Na). b) GCD profiles at 0.1 C; c) Cyclability at 3 C (780 mA g^{-1}); d) Rate capability from 0.2 to 10 C; e) Comparison between the ultra-long cycling curves and coulombic efficiency of the NVO-rGO composite materials with different rGO contents as electrodes for SIBs at 3 C rate (780 mA g^{-1}); f) Rate capability at varied current rates from 0.2 to 10 C for NVO-4% rGO, NVO-9% rGO, and NVO-13% rGO; g–k) Electrochemical performance of NVO-rGO in SIBs: g) CV profiles at scan rate of 0.1 mV s^{-1}; h) GCD curves at 0.1 C (1 C = 260 mA g^{-1}); i) The GCD curves of NVO-rGO from 0.2 to 10 C; j) Cyclability at 1 C (260 mA g^{-1}); k) Ultra-long cyclability and the corresponding coulombic efficiency at 5 C (1300 mA g^{-1}).

capacity (dQ/dV) curves of the NVO-rGO with different rGO contents from the first to the 100th cycle are shown in Figure S6d–f (Supporting Information). Remarkably, Two sets of redox peaks are present at 3.38 and 2.44 V (cathodic), 3.4 and 2.49 V (anodic), as the cycle proceeds, the whole redox peaks are completely overlapping with the subsequent cycles. The redox peaks distinction (potential polarization) are 0.03 and 0.05 V for the NVO-9% rGO, which are lower than those of the NVO (0.11 and 0.14 V), NVO-4% rGO (0.05 and 0.057 V), and NVO-13% rGO (0.06 and 0.075 V), implying its fastest kinetics of redox reactions. It is worth noticing that the oxidation/reduction peaks are evidently overlapped well for the NVO-9% rGO, demonstrating a good reversibility of Na$^+$ intercalation.

To further acquire insight into the impact of rGO percentage on performance, Figure 4e describes the cycling performance of the NVO-rGO with different rGO percentages at 3 C. It can be noticed that the NVO-9% rGO still exhibits the greatest capacity even after ultralong cycling (1000 cycles), while the reversibility increases proportional to the rGO content, i.e., the NVO-13% rGO shows the best reversibility (98.2%) and NVO- 4% rGO the

ADVANCED
SCIENCE NEWS
www.advancedsciencenews.com

ADVANCED
FUNCTIONAL
MATERIALS
www.afm-journal.de

poorest (94.3%). Figure 4f reveals the rate performance of the NVO-rGO with different rGO percentages. All capacities in our research were obtained by virtue of the mass of NVO-rGO. The NVO-rGO with rGO percentage of 9% supplies the highest reversible capacities of 213, 207, 192, 168, and 145 mAh g^{-1} at 0.2 C, 0.5 C, 1 C, 3 C, and 5 C, respectively. Especially at the 10 C, an exceptionally capacity of 100 mAh g^{-1} was retained. Additionally, while current density comes back to 0.2 C, a high capacity of 211 mAh g^{-1} can be restored, demonstrating a superior rate performance of the NVO-9% rGO. It is worth remarking that the performance of the NVO-9% rGO is better than those of 4% and 13% rGO. The reason is that the NVO-rGO with the lower carbon percentage has an inferior conductivity,while the higher carbon percentage can enhance the conductivity but reduce the capacity when used as the cathode. It can be concluded that bonding sites in the low-content rGO composite (NVO-4% rGO) are restricted, while those in NVO-13% rGO hetero-structure that the bonding sites are not completely utilized because the content of active materials was decreased. The conclusion strongly affirm that rGO plays a crucial significant effect in enhancing the electrochemical performance of cathode, implying the necessity of a robust bonding associated between rGO and NVO component. Therefore, the increment of rGO content to a certain extent leads to enhancing of conductivity, contributing to the outstanding rate performance.[41] Herein, with regard to the analyses (Figures S7–S9, Supporting Information), the free-standing NVO-9% rGO electrode displayed the most excellent electrochemical properties among the composite electrodes. Notably, regulating the mass percentage of rGO to 9% in NVO-rGO composite gives rise to an efficient amount of V–O–C bonding sites that can be thoroughly utilized during cycling, affording a superior electrochemical performance.

Figure 4g exhibits the CV profiles of the NVO-9%rGO heterostructure at 0.1 mV s^{-1} for the first three cycles within 1.5–4.0 V (vs Na$^+$/Na). Two relatively conspicuous sharp peaks well overlapped with the subsequent cycles and small distinction between the anodic and cathodic peaks could be assigned to the multistep reversible phase reaction. The intensities for the first three consecutive cycles continuously increase in the following cycles. Meanwhile, the GCD curves of the NVO-9%rGO at 0.1 C exhibit two pairs of distinct plateaus (Figure 4h). This can be obviously discovered that NVO-9%rGO presents a charge/discharge specific capacity of 121/169 mAh g^{-1} during the first cycle (Figure 4h), which indicates that 7.8 mol of Na-ions are inserted into the host and 5.589 mol of Na-ions are extracted. Although the initial coulomb efficiency (ICE) is 72%, it recovers to over 99% and even 100% after the second and 26th cycles, respectively. As a consequence of the activation process, the discharge capacity gradually improves in the first 26 cycles, then obtains the maximum level of 226 mAh g^{-1} (Figure 4h), and preserved the capacity of 215 mAh g^{-1} after 200 cycles with no capacity degradation. Figure 4i presents the GCD curves under different current densities. It further verifies the remarkable rate performance of NVO-9% rGO, and visible voltage plateaus illustrate the fast iontransfer dynamics of the NVO-9% rGO. Moreover, the NVO-9% rGO can present a specific capacity of 192 mAh g^{-1} after 1000 cycles at 1 C (260 mA g^{-1}). Amazingly, it still shows capacity retention of ≈100% (Figure 4j) after 500 cycles, it even shows a slight increase in capacity afterwards. Consequently, the cycle performance presents a great enhancement compared to the NVO material (77.8%, Figure 4j). It indeed displays a stable cyclability with a fairly high specific capacity of 143 mAh g^{-1} at 5 C even after 3000 cycles (1300 mA g^{-1}, 95.8% capacity retention).

To thoroughly probe the prior mentioned excellent performance, the kinetics were well-researched through the redox pseudo-capacitance-like and galvanostatic intermittent titration technique (GITT). The kinetics of Na$^+$ storage for the NVO-9% rGO was further probed by multi-sweep rate CV curves. The CV profiles acquired at varied scan rates varying from 0.1 to 1.0 mV s^{-1} are displayed in **Figure 5**a. With increasing the sweep speed, primary oxidation peaks in the curves switch to higher regions, meanwhile the reduction peaks shift to lower ones. Principally, the association between the peak current (i) and sweep speed(v) could be quantified based upon the formula: $i = av^b$, where the b value closing to 0.5 exhibits an ionic diffusion-controlled procedure, when closing to 1.0 indicates a capacitive nature.[42–46] The b values of peak I, II, III, and IV of the NVO-9%rGO are more than 0.5 (Figure 5b), implying that surface-induced pseudo-capacitive behavior is the predominant electrochemical reaction during Na$^+$ storage process. It is worth noticing that these values are bigger than other two electrodes (Figures S8 and S9, Supporting Information). The NVO-9% rGO presents the pseudo-capacitance contributions of 74.9%, 81.2%, 85.4%, 89.5%, and 93.8% at 0.2, 0.4, 0.6, 0.8, and 1 mV s^{-1}, respectively (Figure 5d). The capacitive percentage of the current in NVO-9% rGO heterostructures is 74.9% at 0.2 mV s^{-1}, which heightens to 93.8% at 1.0 mV s^{-1} (Figure 5d). The ultrahigh capacitive contribution implies a unique pseudo-capacitive effect, which could be ascribed to the interface-controlled reaction processes. The kind of capacitivecontrolled progress brings about the rapid kinetics in the NVO-9% rGO heterostructures. Particularly, the b-value of the extra reduction peak for the NVO-9% rGO is close to 1 (Figure 5b). These values demonstrate a high pseudo-capacitive percentage among the charge and discharge processes of the cathodes. The representative voltage curves of the five samples for calculated pseudocapacitive current related to the measured current are also displayed for comparison in Figure S8g (Supporting Information). It can be noticed that the surface-capacitive influence of the NVO-9% rGO with a controllable composition is more critical than the other samples.

The storage kinetics of Na$^+$ in NVO-9% rGO was evaluated as well by the GITT over the charge/discharge processes (Figure 5e) to clarify the effect of multi-step sodiation/desodiation reaction of NVO-9% rGO on the ion diffusion and conductivity properties. The D_{Na+} values of NVO-9% rGO during the charging/discharging process are measured (i.e., ≈10^{-11} to 10^{-12} cm^2 s^{-1}) and accordingly depicted in Figure 5f, which are higher than those in the V-based cathodes.[9,12,14] The boosted capacitive contributions and decent kinetics are assigned to the formation of V–O–C bonding with the introduction of rGO, giving rise to the superior rate capability and fast charge-transfer kinetics for the NVO-9% rGO. Moreover, to obtain insights into the electrode process kinetics of the NVO-rGO, NVO/rGO, and NVO, the diffusion coefficient of Na$^+$ in the NVO-rGO was experimentally determined to be 10^{-11} cm^2 s^{-1} through the GITT measurements (Figure S10, Supporting Information). Obviously, the calculation results agree well with the experimental ones, which are two orders of magnitude larger than those reported.[9,12,14]
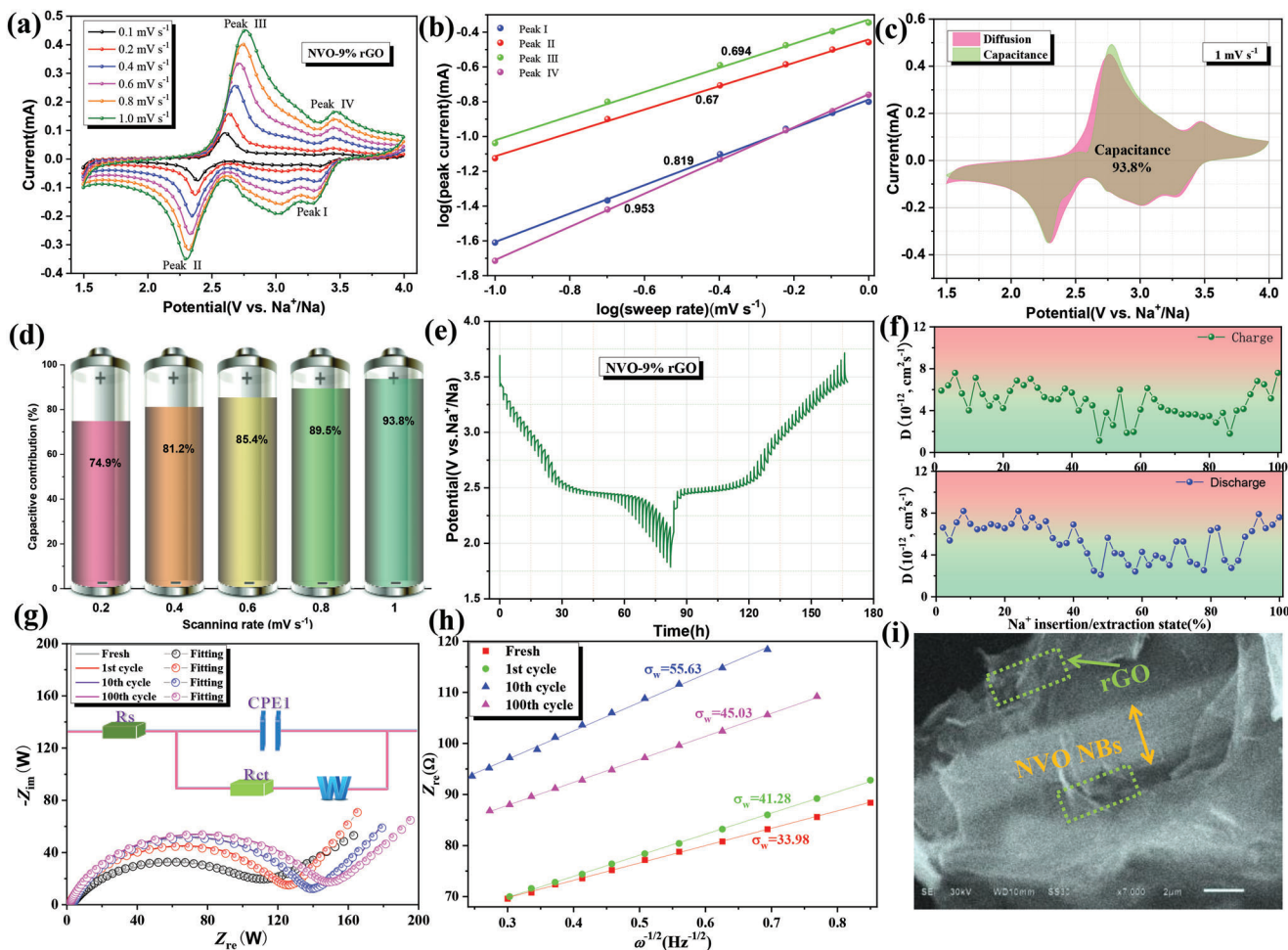
**ADVANCED
SCIENCE NEWS**

www.advancedsciencenews.com

**ADVANCED
FUNCTIONAL
MATERIALS**

www.afm-journal.de

Figure 5. Electrochemical kinetics analysis of the Na$^+$ storage nature of the NVO-rGO electrode: a) CV profiles at varied scan speeds from 0.1 to 1.0 mV s^{-1}. b) The linear relationship of log(i) versus log(v) plots for cathodic and anodic peaks of NVO-rGO; c) Capacitive contribution (green shaded region) of NVO-rGO acquired at 1.0 mV s^{-1}, and d) The percentage of measured pseudocapacitive contribution at 0.2–1.0 mV s^{-1}; e) GITT curves for the NVO-rGO; f) The Na$^+$ diffusion coefficient of NVO-rGO sample during charge and discharge. g) Nyquist patterns, and h) The Z_{re} versus $\omega^{-1/2}$ lines of the NVO-rGO electrode before cycling, and at the fully charged after different cycling at 0.1 C rate for 1, 10, and 100 cycles. i) Surface SEM patterns of the NVO-rGO after 100 cycles at 0.1 C.

The electrochemical impedance spectroscopy (EIS) experiments at different stages (1st, 10th, and 100th cycles) were also executed to further identify the discharge and charge characteristics. It is noticed that the charge-transfer resistance in the 1st, 10th, and 100th cycles exhibit an increase compared to that before cycling. The small resistance and σ value of the initial cathode would imply the good electronic conductivity of the NVO-rGO sample (Figure 5g,h). During the following cycles, the charge-transfer resistance increases, but only a slight amount, this is chiefly due to the constant deposition of sodium ion in SEI film. According to the SEM patterns from the appearance of the NVO-rGO after 100 cycles (Figure 5i), the configuration of the electrode remains basically intact and similar to its original state without any serious damage after cycling. The result further affirms the fast charge-transfer, superior electron conductivity and excellent reaction kinetics for Na-ion storage in the electrode, occurring by the introduction of appropriate amount of graphene to accelerate the formation of appropriate V–O–C bonding.

Through density functional theory (DFT) calculation combined with the relevant experimental data to further analyze the interfacial interaction of NVO-rGO heterostructures, it was demonstrated that the Mulliken charge of interfacial V improves attribute to the construction of interfacial V–O–C bonds. First, the diffusion characteristics of Na$^+$ ions at the hetero-interface were further revealed, the perfect diffusion routes for the NVO-rGO and NVO samples are supplied in **Figure 6**a,b, respectively. In the NVO, two characteristic sodium-diffusion paths were examined in Figure 6c. The energy barriers for path 1, 2 were 0.46 and 0.45 eV, respectively. The diffusion energy barrier associated with V–O–C interfacial pathway process of the NVO-rGO heterostructures are 0.30 and 0.31 eV, which is much lower than that of the NVO (0.46 eV). Particularly, much more feasible pathways could be formed at bonded the NVO-rGO interface in the hybrid, implying a dramatically enhanced diffusion kinetics and fast Na$^+$ diffusion path. Namely, Na$^+$ ions are favorable in the V–O–C bonding interface. Second, we have
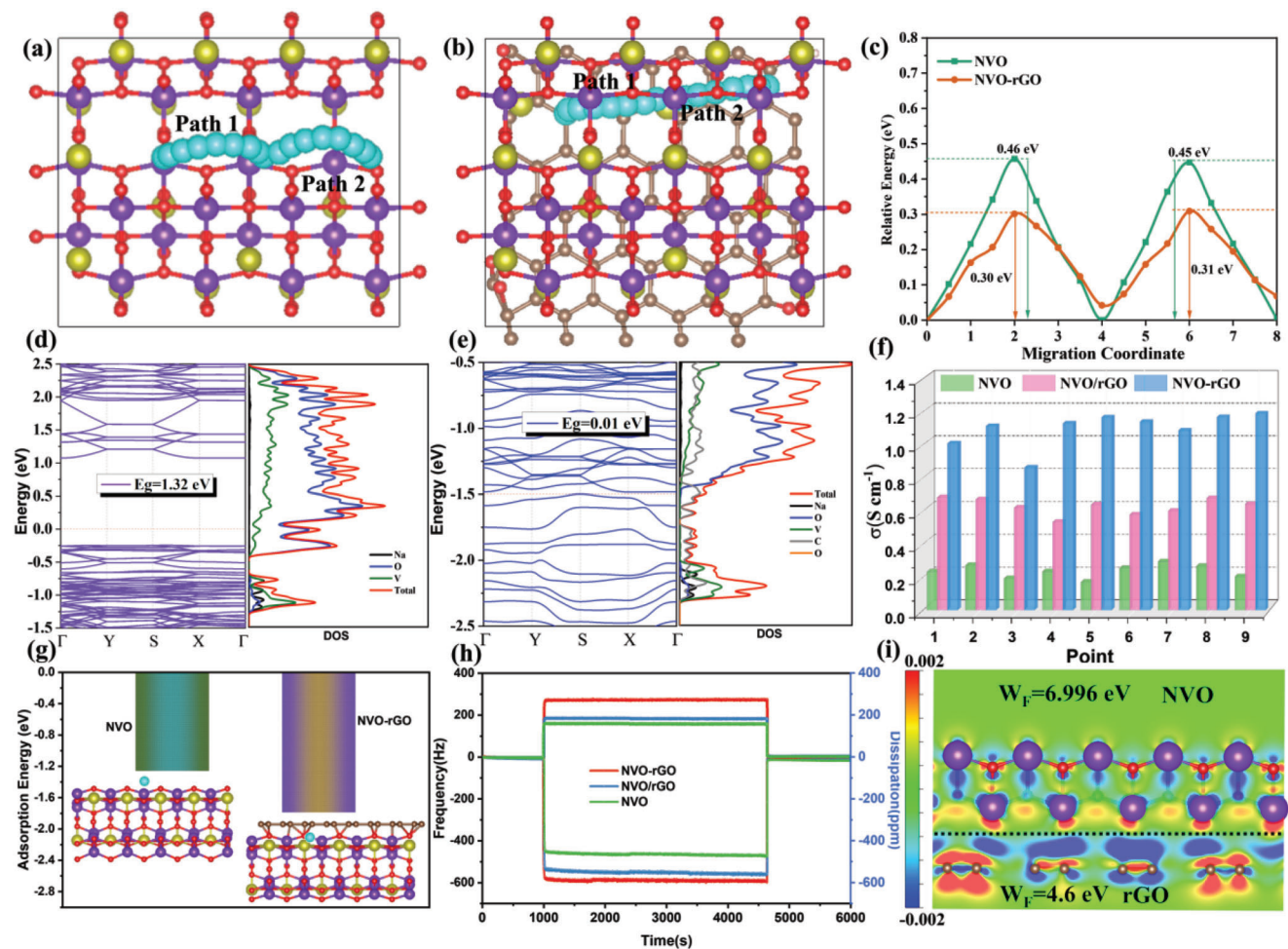
Figure 6. a,b) Na-ion migration pathways; c) The migration energy barriers in the bare NVO and NVO-rGO heterostructure; d,e) The calculated band structure and density of states for d) NVO and e) NVO-rGO. f) Electrical conductivity of the NVO, NVO/rGO, and NVO-rGO. g) Calculated sodium ion adsorption energies of NVO and NVO-rGO. h) Electrochemical quartz crystal microbalance frequency response. i) The difference in charge density of NVO-rGO heterostructure. Yellow, red, brown, and purple balls represented Na, O, C, and V atoms, respectively.

calculated the band structure and density of states (DOS) to explore the electronic structure of NVO-rGO hetero-structure. As displayed in Figure 6d, there is a large bandgap of 1.32 eV for NVO calculated by the Perdew-Burke-Ernzerhof approach, decreasing the bandgap to 0.01 eV as compared with pristine NVO. Revealing that a semi-conductive feature of NVO. With the introduction of V-O-C bonding which can reduce the bandgaps to further enhance electrical conductivity. The bandgap fades and changes into a conductor property, the band structure of the NVO-rGO heterostructures is successful across the Fermi level by the electron transfer in Figure 6e, thereby increasing the electronic conductivity.[47–52] Conductivity test results also verify NVO-rGO which has superior conductivity, the same order of magnitude but much higher than NVO (Figure 6f), in agreement with the DFT result. Such results have demonstrated the significance of creating hetero-structure of NVO-rGO in enhancing the overall electronic and ionic conductivity compared with the NVO, concurrently. Furthermore, to further demonstrate the effect of V−O−C interfaces behavior on reaction kinetics. The optimized Na+ adsorption model accompanied by the calculated NVO ad-

sorption energies of and NVO-rGO were established, the Na+ adsorption energies (Eads) of NVO-rGO and NVO are also calculated and the results are depicted in Figure 6g. By engineering an attractive V-O-C interface, the sodium ion adsorption energy of NVO-rGO (−1.796 eV) is much lower than NVO (−1.265 eV), implying that the NVO-rGO heterostructures are more favorable for the adsorption of sodium ions and favorable for the improvement of sodium storage capacity. As presented in Figure 6h, electrochemical quartz crystal microbalance (EQCM) was illustrated to identify the Na+ adsorption on NVO-rGO heterostructures in neat ionic liquid. The oscillation frequency is closely connected to the viscoelastic switches and mass transport in the electrode. Comparatively, both frequency and dissipation signals reverted to the initial states, illustrating that the viscoelastic and quality alterations were completely recoverable. This is in accordance with the conclusions in Figure 6g. Considering that the above results might be induced by the interfacial charge distribution between different phases, as presented in Figure 6i, where the red and blue iso-surfaces denote the accumulation and depletion of electron density, respectively. The work functions of single layer NVO
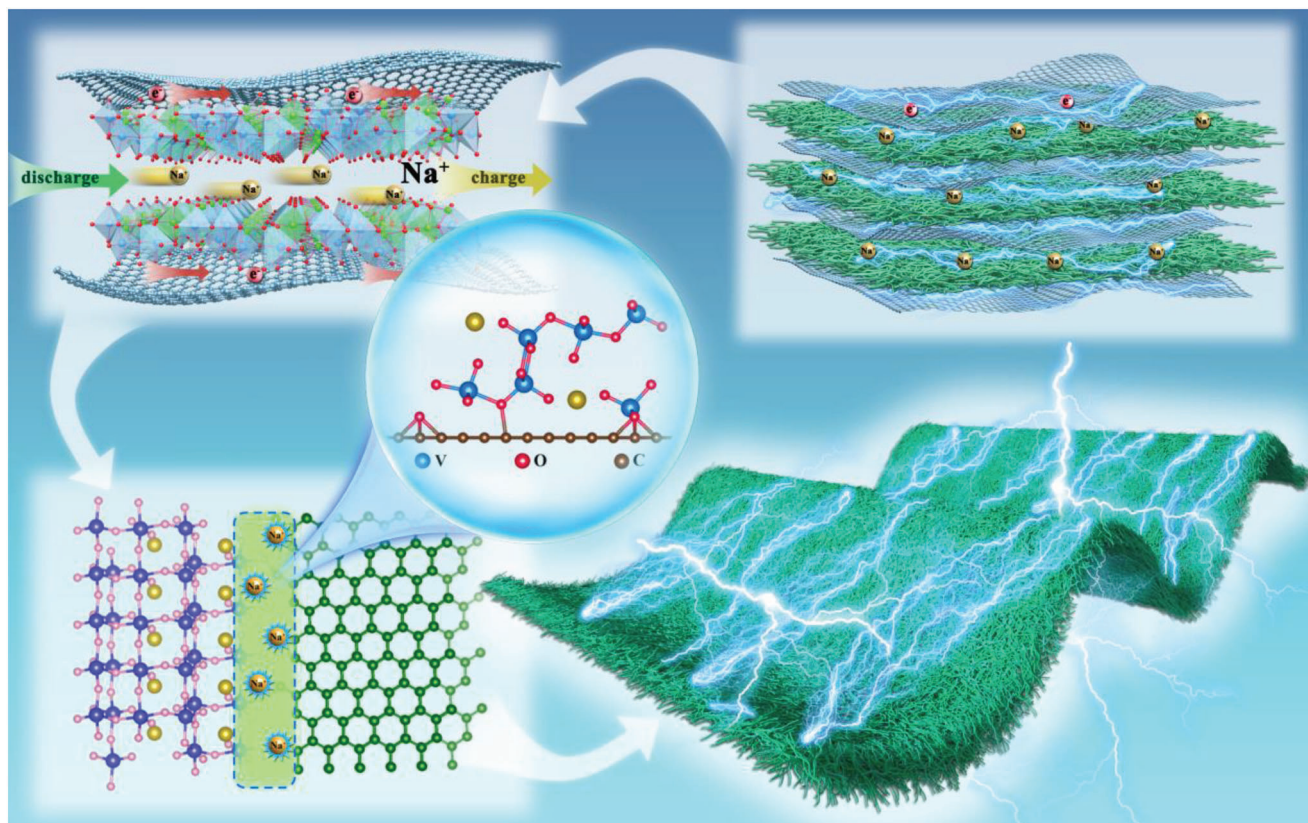
**ADVANCED
SCIENCE NEWS**
www.advancedsciencenews.com

**ADVANCED
FUNCTIONAL
MATERIALS**
www.afm-journal.de

Figure 7. Schematic diagram of the free-standing NVO-rGO heterointerface with V−O−C bond and its anomalous Na$^+$ storage principle.

and rGO are 6.996 and 4.6 eV, respectively. Apparently, built-in electric field at the V−O−C bonding interface pointing from rGO toward NVO is constructed. The Bader analysis illustrate that electrons are focused on the interfacial V−O−C bond, which strongly attract Na$^+$ on NVO side. The interior stress field at interface can forward the Na$^+$ and remarkably hasten the charge transfer kinetics. Both experiment and DFT calculation results demonstrate the electronic structure on the interface has been modified, which also agrees well with the result in our analysis presented in Figure 1.

According to the above analysis, a feasible mechanism for the comprehended powerful improvement for the course of reaction was presented as revealed in **Figure 7**. Owing to the difference of Fermi levels in the NVO and rGO,[50] propelled by the huge potential energy distinction, electrons instinctively transfer from the higher level to the lower one at the V−O−C interface while the two materials connect, which allows the formation of a "sodium reservoir". The large compression gradient at the V−O−C interface accelerates the distribution of sodium ions to both edges of the interface, acquiring excellent diffusion kinetics. Meanwhile, the charge restructuring can boost the electron motion.[46,51−53] Accordingly, our theoretical research indicates that formation of the robust interfacial electronic interaction of V−O−C bonds at the interface between the NVO and rGO not only generate additional active sites, but also accelerates ion migration to promote the charge-transfer kinetics. Indeed, the bonding interface (NVO-rGO) anchors Na$^+$ ions more tightly than surface sites (NVO/rGO), make the interface storage more beneficial in prac-

tice. Such immense improvements in the membranes can be explicated by the following viewpoints. First, the formation of V-O-C bonding ensures the tight bonding between the NVO and rGO as revealed in Figure 7. Second, the well-crystallized culture mode improves the distribution of rGO NSs in the NVO NBs, benefiting from the appropriate crosslinking within the NVO NBs, which produces a high compressive strength and accelerates the mechanical binding of the two materials. Therefore, strong V-O-C bonding, the built-in electric field and even distribution are the critical conditions responsible for the tremendous enhancements in mechanical properties of the membranes.

To deeply explore the structural variations of the NVO-9% rGO under different charging/discharging stages upon Na$^+$ ion extraction/insertion, in situ and ex situ XRD measurements were executed. **Figure 8**a,b show the in situ XRD images recorded for the original two cycles. All the patterns produce almost coinciding characteristic peaks with almost unchanged positions. Notably, no additional diffraction peaks are detected when the initial sodium extraction/insertion (Figure 8a). The structural transformations during the second cycles, and the enlargements of certain angular ranges in contour maps are presented in Figure 8b,c. All characteristic diffraction peaks exhibit the same trend of transformation, implying a superb structural robustness of the NVO crystalline skeleton. The peaks of (001) and (401) gradually shift to lower angle while (300), (102), (−410), and (−401) peaks move to higher angle (Figure 8c). They shift to higher angle through charging, vice versa during discharging, matching with the lattice compression and expanding,
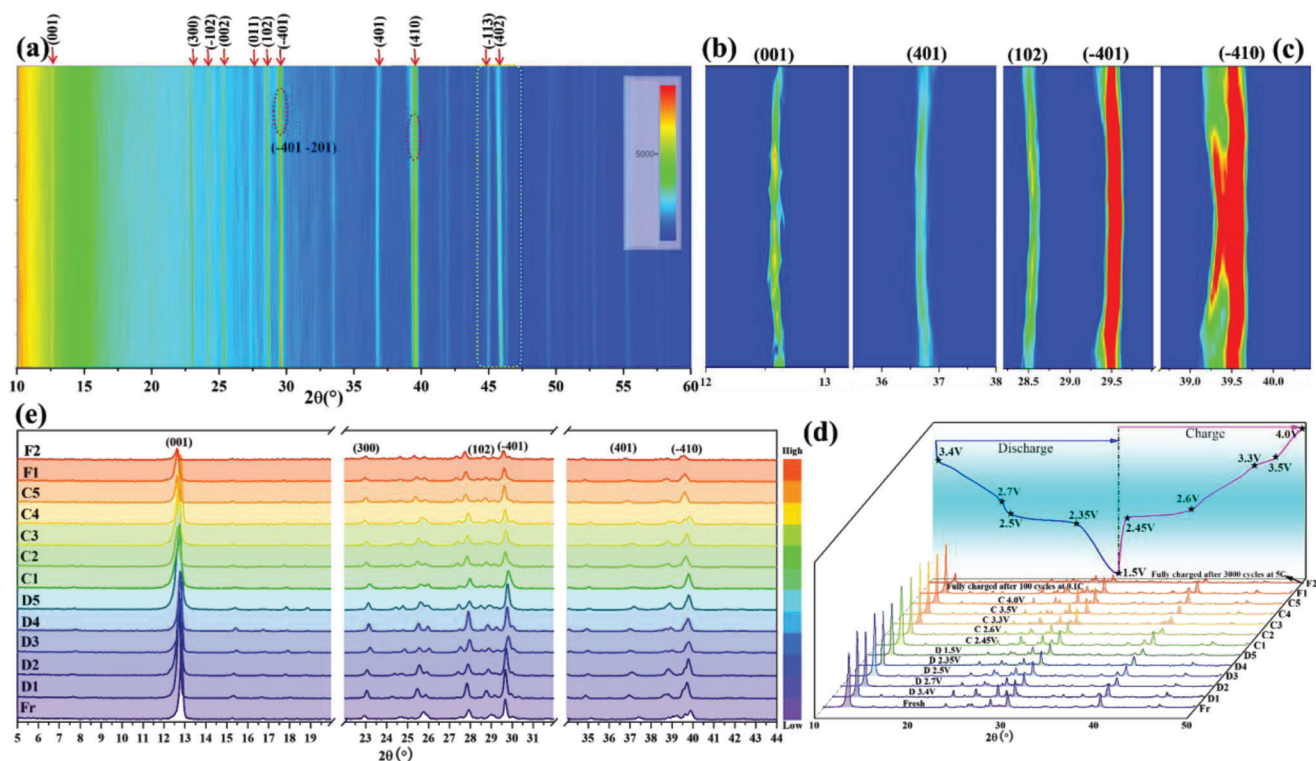
2303211 (11 of 15)

Figure 8. Structural characterizations of the NVO-9% rGO; a) In situ X-ray diffraction (XRD) patterns of the NVO-9% rGO electrode for the SIBs charge/discharge for the first and second cycles at 20 mA g^{-1}; b,c) The corresponding 3D graphs displaying the conversion of the main characteristic diffraction peaks during the second cycle for NVO-9% rGO electrode; d,e) Ex situ XRD patterns and GCD curves of the NVO-9% rGO under different working states(Fr-F2) for the second cycle even after 100 cycles at 0.1 C rate.

respectively. Thus, the peak position only shifts slightly during the total process and no new peak is generated. Furthermore, these peaks undergo an exact opposite variation and finally come back to their original states after a whole cycle, which manifests the high reversibility and accounts for the superb cyclability (95.4%, 3000 cycles at 5 C). The regular peak move and lattice alteration are suggestive of a single phase which can be recognize across the entire charge and discharge procedure, thereby illustrating a representative solid-solution reaction process. Meanwhile, the ex situ XRD collected at different charge/discharge circumstance after several cycles are gathered and compared in Figure 8d,e, exhibiting highly similar shapes, which are consistent with the former XRD results. It confirms that c axis is broadening, a/b plane is compression assignable to the expanded electrostatic repulsion among neighboring oxygen layers, thereby facilitating the formation of V—O—C bonding. Moreover, it should be noticed that the corresponding peak moves are totally reversible during sodium ion is embedded back to crystal lattice, implying an accommodating volumetric variation and excellent reversibility among the extraction/insertion of Na ions. Therefore, an enhanced capacity contribution, even more exceptional Na$^+$ diffusion channels ascribe to the enlarged Na$^+$ layers spacing. This would efficiently assure a excellent structural stability for NVO-rGO through cycling, resulting in its superior cycling performance.

The superior electrochemical properties of the NVO-rGO prompted us to research the performance of full-cell. **Figure 9**

illustrates the structure and flexible nature of the as-prepared electrode. To research the flexibility systematically, a pouch cell was assembled employing the NVO-rGO free-standing cathode as depicted in the schematic diagram in Figure 9a. The assembled soft packing vehicle was curved under irregular curving angles. As shown in Figure 9b,c, a light-emitting diode and LED lamp were successfully lit by the full-cell. The packing was unaffected to the blending procedures and can be bended in 90°, 180°, 360° and even more rolled up position without any evident alter in the light-emitting diode (LED), demonstrating a superior flexible properties and electrochemical performance under the normal and folded states. Moreover, two different sets of anodes, i.e., electrochemically presodiated rGO as well as presodiated hard carbon, were used in the full-cells to countervail Na$^+$ ions consumption during the course of the emergence of SEI film. To explore the flexibility of the NBs array based NVO-rGO //rGO and NVO-rGO//hard carbon full-cell for comparison(between fully flexible and traditional electrodes). Notably, the NVO-rGO//rGO full-cell transfer a striking cyclability with capacity retaining of 90% and stable coulombic efficiency (>90%) after 200 cycles at 200 mA g^{-1} (Figure 9d), NVO-rGO//hard carbon full-cell delivers a capacity retention of 93.7% and stable coulombic efficiency after 500 cycles at 200 mA g^{-1} (Figure 9e). This outstanding performance of the flexible NVO-9% rGO can be associated to the distinctive architectures. First, the NVO NBs and rGO NSs are tightly blended which enables an adequate attachment and electrical junction, driving to a rapid electron transfer between the NVO-rGO and
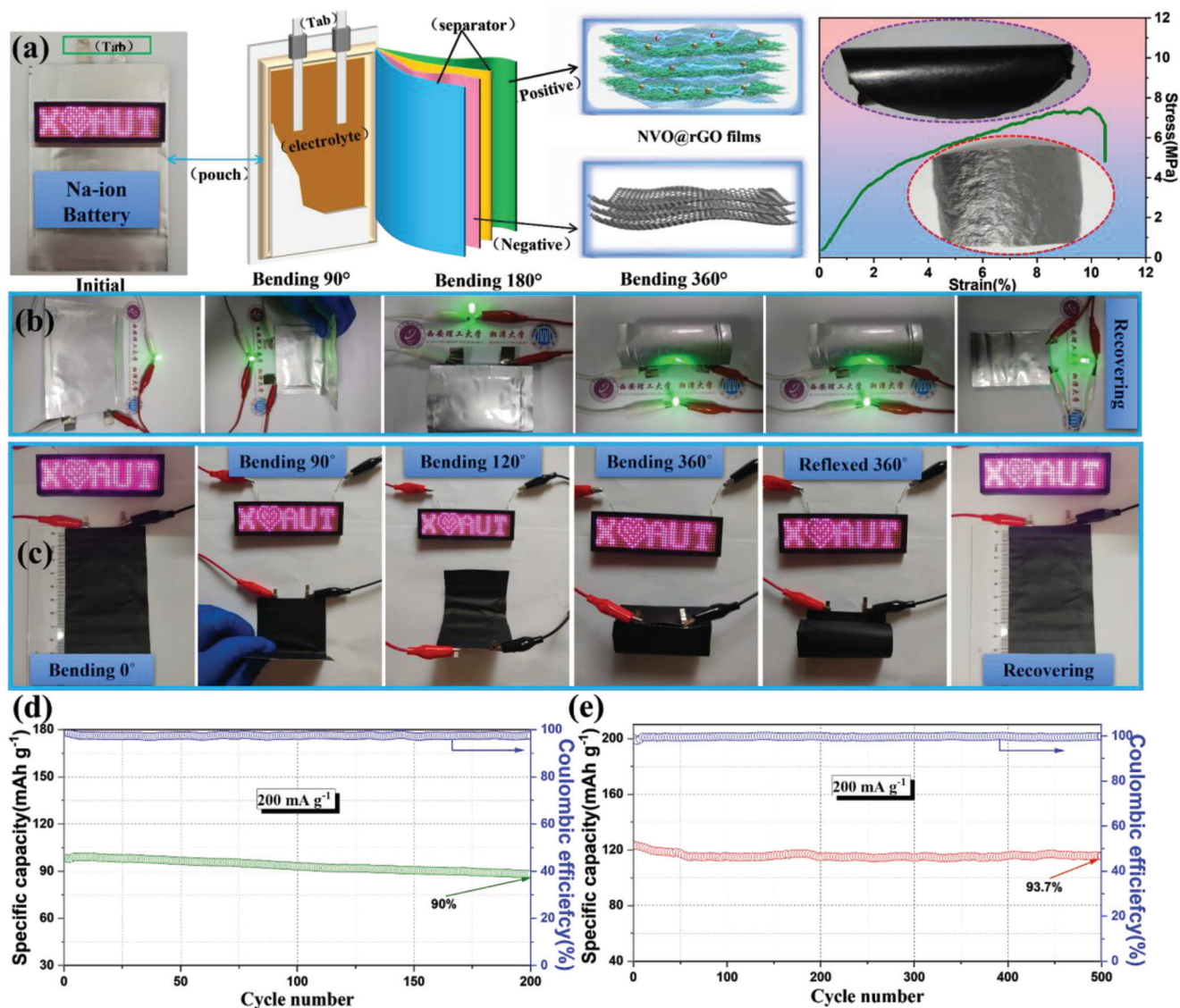
**ADVANCED
SCIENCE NEWS**

www.advancedsciencenews.com

**ADVANCED
FUNCTIONAL
MATERIALS**

www.afm-journal.de

Figure 9. Structure and bending properties of the flexible sodium-ion full-cell (cathode: free-standing NVO-rGO; anode: presodiated graphite; electrolyte: 1.0 M $NaClO_4$ in EC/DEC (1:1) with 5%FEC; a) Schematic diagram for construction of the flexible Na-ion pouch cell and corresponding structure; b) Digital images of the bendable full-cell illuminating LED under different states and picture of LED lighted by the pocket full-cell (presodiated rGO as anode). c) LED screen lighted by the pouch full-cell (presodiated hard carbon as anode). d,e) Cyclical stability of the full-cell device at 200 mA g^{-1}; cathode: NVO-rGO; anode: presodiated rGO and hard carbon.

substrate as well as excellent flexibility. Second, the freestanding NVO-9% rGO can accelerate the electrolyte infiltration and offer a appropriate sites for buffering the volume-change among sodiation/desodiation, promoting rapid ion delivery and excellent mechanical property. Finally, the NVO-rGO heterostructure can largely reduced Na$^+$ diffusion range and enlarge the surface area, consequently acquiring a great applying of the active material and a superb rate performance. Although, in the absence of binders, the designed V−O−C chemical bonding between rGO and NVO accelerates the charge delivery and defenses the enormous stain under extending. The designed chemical bonding is regarded as the crucial strategy to fulfil the mechanical demands for the flexible sodium-ion battery.

3. Conclusion

To summarize, this research has comprehensively explored the V−O−C bonding hetero-interfacial predominant Na$^+$ storage behavior in the free-standing NVO-rGO heterostructure by performing a series of investigations. The predominantly interfacial Na$^+$ storage mechanism exhibits superior performance toward NVO and rGO compared to the conventional systems attributed to the formation of bonding and the creation of stress fields, favors NVO-rGO with potential of faradaic-active energy storage. The DFT simulations supply a viewpoint of the greater diffusion kinetics and extra storage situations of Na$^+$ at the interface of NVO-rGO compared to the NVO/rGO and NVO

2303211 (13 of 15)

cathodes. The construction of V–O–C bonding provides a thoroughfare for rapid ion transport, and a substantial available region for electrochemical reactions. Benefiting from the V–O–C hetero-interfacial mechanism, NVO-9% rGO provides more active and plentiful Na^+ storage ability, satisfactory capacity, striking cycling stability, superior rate capability, superb mechanical properties coupled with an outstanding capacitive behavior. This approach markedly optimized the conventional preparation procedure, as well as perfectly preserved the fascinating interconnected network throughout the entire electrode, enabling the NVO-rGO with prominent integrity in SIBs. Moreover, the interfacial NVO-9% rGO heterostructure displays a high capacity of 158 mAh g^{-1} at 1300 mA g^{-1} (5 C) with extraordinary rate capability of 100 mAh g^{-1} at 10 C. The exceptional electrochemical characteristics demonstrate the synergistic nature that interfacial chemical bond construction and the built-in electric field in boosting the performance of $Na_5V_{12}O_{32}$-based cathodes in SIBs. The results demonstrate that the free-standing NVO-rGO is a highly valuable cathode for high-energy-density sodium ion batteries, as well as develops another approach to design advanced materials for further applying in more energy storage systems.

Supporting Information

Supporting Information is available from the Wiley Online Library or from the author.

Conflict of Interest

The authors declare no conflict of interest.

Data Availability Statement

The data that support the findings of this study are available from the corresponding author upon reasonable request.

[1] M. Chen, Q. Liu, Z. Hu, Y. Zhang, G. Xing, Y. Tang, S. L. Chou, *Adv. Energy Mater.* **2020**, *10*, 2002244.

[2] X. Liu, H. Zhang, D. Geiger, J. Han, A. Varzi, U. Kaiser, A. Moretti, S. Passerini, *Chem. Commun.* **2019**, *55*, 2265.

[3] Y. Cheng, Y. Xia, Y. Chen, Q. Liu, T. Ge, L. Xu, L. Mai, *Nanotechnol.* **2019**, *30*, 192001.

[4] B. Lza, B. Wla, B. Lxa, Y. Qi, B. Xca, *Chem. Eng. J.* **2019**, *372*, 1056.

[5] Q. Zhou, L. Wang, W. Li, K. Zhao, M. Liu, Q. Wu, Y. Yang, G. He, I. P. Parkin, P. R. Shearing, D. J. L. Brett, J. Zhang, X. Sun, *Electrochem. Energy Rev.* **2021**, *4*, 793.

[6] F. Hu, D. Xie, F. H. Cui, D. X. Zhang, G. H. Song, *RSC Adv* **2019**, *9*, 20549.

[7] X. Song, J. Li, Z. Li, Q. Xiao, G. Lei, Z. Hu, Y. Ding, H. M. Kheimeh Sari, X. Li, *ACS Appl. Mater. Interfaces* **2019**, *11*, 10631.

[8] X. Song, J. Li, Z. Li, X. Li, Y. Ding, Q. Xiao, G. Lei, *Acta Chim. Sin.* **2019**, *77*, 625.

[9] Y. Dong, S. Li, K. Zhao, C. Han, W. Chen, B. Wang, L. Wang, B. Xu, Q. Wei, L. Zhang, *Energy Environ. Sci.* **2015**, *8*, 1267.

[10] E. Uchaker, H. Y. Jin, P. Yi, G. Z. Cao, *Chem. Mater.* **2015**, *27*, 7082.

[11] S. Yuan, X. Liu, X. Dan, D. Ma, X. Zhang, *Adv. Sci.* **2015**, *2*, 1400018.

[12] A. Radwan, Y. Liu, Y. Qi, W. Jin, V. Nguyen, X. Yang, S. Yang, W. Chen, *Mater. Res. Bull.* **2018**, *97*, 24.

[13] S. Hartung, N. Bucher, J. B. Franklin, A. M. Wise, L. Y. Lim, H. Y. Chen, J. N. Weker, M. E. Michel Beyerle, M. F. Toney, M. Srinivasan, *Adv. Energy Mater.* **2016**, *6*, 1502336.

[14] A. R. Radwan, Y. Liu, V. Nguyen, W. Chen, *J Mater Sci* **2018**, *29*, 7032.

[15] H. Kang, Y. Liu, M. Shang, T. Lu, Y. Wang, L. Jiao, *Nanoscale* **2015**, *7*, 9261.

[16] H. He, G. Jin, H. Wang, X. Huang, Z. Chen, D. Sun, Y. Tang, *J. Mater. Chem. A* **2014**, *2*, 3563.

[17] S. Osman, S. Zuo, X. Xu, J. Shen, Z. Liu, F. Li, P. Li, X. Wang, J. Liu, *ACS Appl. Mater. Interfaces* **2021**, *13*, 816.

[18] X. Kuai, K. Li, J. Chen, H. Wang, J. Yao, C. L. Chiang, T. Liu, H. Ye, J. Zhao, Y. G. Lin, *ACS Nano* **2022**, *16*, 1502.

[19] B. Ge, J. Wang, Y. Sun, J. Guo, Q. Peng, *ACS Appl. Energy Mater.* **2020**, *3*, 3789.

[20] Z. Wang, Y. Zhang, H. Jiang, C. Wei, Y. An, L. Tan, S. Xiong, J. Feng, *Nano Res.* **2023**, *16*, 458.

[21] H. Shan, J. Qin, Y. Ding, H. Sari, X. Song, W. Liu, Y. Hao, J. Wang, C. Xie, J. Zhang, *Adv. Mater.* **2021**, *33*, 2102471.

[22] Y. Li, J. Qian, M. Zhang, S. Wang, Z. Wang, M. Li, Y. Bai, Q. An, H. Xu, F. Wu, L. Mai, C. Wu, *Adv. Mater.* **2020**, *32*, 2005802.

[23] Y. Chen, J. Zhang, M. Li, C. Yang, L. Zhang, C. Wang, H. Lu, *Electrochim. Acta* **2018**, *292*, 115.

[24] S. Osman, C. Peng, F. Li, H. Chen, J. Shen, Z. Zhong, W. Huang, D. Xue, J. Liu, *Adv. Sci.* **2022**, *9*, 2205575.

[25] S. Hu, Y. Li, Y. Chen, J. Peng, T. Zhou, W. K. Pang, C. Didier, V. K. Peterson, H. Wang, Q. Li, *Adv. Energy Mater.* **2019**, *9*, 1901795.

[26] B. Huang, S. Liu, X. Zhao, Y. Li, J. Yang, Q. Chen, S. Xiao, W. Zhang, H. E. Wang, G. Cao, *Sci. China Mater* **2021**, *64*, 85.

[27] H. Jiang, D. Ren, H. Wang, Y. Hu, S. Guo, H. Yuan, P. Hu, L. Zhang, C. Li, *Adv. Mater.* **2015**, *27*, 3687.

[28] C. J. Chen, H. H. Xu, T. F. Zhou, Z. P. Guo, L. N. Chen, *Adv. Energy Mater.* **2016**, *6*, 1600322.

[29] C. Chen, J. Maier, *Nat. Energy* **2018**, *3*, 102.

[30] C. Chen, Y. Wen, X. Hu, X. Ji, M. Yan, L. Mai, P. Hu, B. Shan, Y. Huang, *Nat. Commun.* **2015**, *6*, 6929.

[31] A. Chen, X. Yu, Y. Zhou, S. Miao, Y. Li, S. Kuld, J. Sehested, J. Liu, T. Aoki, S. Hong, M. F. Camellone, S. Fabris, J. Ning, C. Jin, C. Yang, A. Nefedov, C. Wöll, Y. Wang, W. Shen, *Nat. Catal.* **2019**, *2*, 334.

[32] D. Yu, Z. Wei, X. Zhang, Y. Zeng, C. Wang, G. Chen, Z. X. Shen, F. Du, *Adv. Funct. Mater.* **2021**, *31*, 2008743.

[33] J. Lee, K. S. Novoselov, H. S. Shin, *ACS Nano* **2011**, *5*, 608.

[34] D. Kong, X. Li, Y. Zhang, X. Hai, B. Wang, X. Qiu, Q. Song, Q. H. Yang, L. Zhi, *Energy Environ. Sci.* **2016**, *9*, 906.

[35] G. Yang, W. Hou, Z. Sun, Q. Yan, *J. Mater. Chem. A* **2005**, *15*, 1369.

[36] S. H. Lee, H. M. Cheong, M. J. Seong, P. Liu, C. E. Tracy, A. Mascarenhas, J. R. Pitts, S. K. Deb, *J. Appl. Phys.* **2002**, *92*, 1893.

**ADVANCED
SCIENCE NEWS**

www.advancedsciencenews.com

**ADVANCED
FUNCTIONAL
MATERIALS**

www.afm-journal.de

[37] Y. Dai, X. Liao, R. Yu, J. Li, J. Li, S. Tan, P. He, Q. An, Q. Wei, L. Chen, X. Hong, K. Zhao, Y. Ren, J. Wu, Y. Zhao, L. Mai, *Adv. Mater.* **2021**, *33*, 2100359.

[38] S. Osman, C. Peng, J. Shen, F. Li, W. Huang, J. Liu, J. Liu, D. Xue, M. Zhu, *Nano Energy* **2022**, *100*, 107481.

[39] C. Y. Foo, A. Sumboja, D. Tan, J. Wang, P. S. Lee, *Adv. Energy Mater.* **2014**, *4*, 1400236.

[40] Y. Zhang, Y. Wang, Z. Xiong, Y. Hu, W. Song, Q. A. Huang, X. Cheng, L. Q. Chen, C. Sun, H. Gu, *ACS Omega* **2017**, *2*, 793.

[41] T. Jin, Y. Liu, Y. Li, K. Cao, X. Wang, L. Jiao, *Adv. Energy Mater.* **2017**, *7*, 1700087.

[42] B. Yin, S. Liang, D. Yu, B. Cheng, I. L. Egun, J. Lin, X. Xie, H. Shao, H. He, A. Pan, *Adv. Mater.* **2021**, *33*, 2100808.

[43] D. Bin, W. Huo, Y. Yuan, J. Huang, Y. Liu, Y. Zhang, F. Dong, Y. Wang, Y. Xia, *Chem.* **2020**, *6*, 968.

[44] N. Zhang, M. Jia, Y. Dong, Y. Wang, J. Xu, Y. Liu, L. Jiao, F. Cheng, *Adv. Funct. Mater.* **2019**, *29*, 1807331.

[45] H. Chen, J. Huang, S. Tian, L. Liu, T. Qin, L. Song, Y. Liu, Y. Zhang, X. Wu, S. Lei, S. Peng, *Adv. Sci.* **2021**, *8*, 2004924.

[46] F. Zeng, M. Yu, W. Cheng, W. He, Y. Pan, Y. Qu, C. Yuan, *Small* **2020**, *16*, 2001905.

[47] B. Kang, S. Lim, W. H. Lee, S. B. Jo, K. Cho, *Adv. Mater.* **2013**, *25*, 5856.

[48] J. Wang, Z. Wang, J. Ni, L. Li, *Electrochem. Energy Rev.* **2022**, *5*, 211.

[49] Y. Y. Hsieh, H. Y. Tuan, *Energy Storage. Mater.* **2022**, *51*, 789.

[50] C. Ke, R. Shao, Y. Zhang, Z. Sun, S. Qi, H. Zhang, M. Li, Z. Chen, Y. Wang, B. Sa, H. Lin, H. Liu, M. S. Wang, S. Chen, Q. Zhang, *Adv. Funct. Mater.* **2022**, *32*, 2205635.

[51] Y. Lin, L. Yang, Y. Zhang, H. Jiang, Z. Xiao, C. Wu, G. Zhang, J. Jiang, L. Song, *Adv. Energy Mater.* **2018**, *8*, 1703623.

[52] L. Fang, Z. Lan, W. Guan, P. Zhou, N. Bahlawane, W. Sun, Y. Lu, C. Liang, M. Yan, Y. Jiang, *Energy Storage Mater.* **2019**, *18*, 107.

[53] H. Wang, K. Xie, Y. You, Q. Hou, K. Zhang, N. Li, W. Yu, K. P. Loh, C. Shen, B. Wei, *Adv. Energy Mater.* **2019**, *9*, 1901806.